# Rapid Simulation of Photonic Integrated Circuits using Verilog-A Compact Models

Md Jubayer Shawon, Student Member, IEEE, and Vishal Saxena, Member, IEEE,

Abstract—Silicon-based electronic-photonic integration offers several opportunities for integrated circuits (IC) designers to innovate systems architectures that leverage the advantages of optical-domain signal processing and low-loss transmission in optical fibers. However, photonic integrated circuit (PIC) design tools have evolved from the numerical Maxwell field solvers and are completely disjointed from the electronic circuit simulation tools such as SPICE and Cadence Spectre. Thus there is a gap that needs to be filled by the IC community where they can instantiate photonic building blocks to form PICs and perform co-simulation with interfacing (Bi)CMOS electronic circuits. In recent work, Verilog-A compact models have been developed for photonic device building blocks that enable transient simulations of hybrid electronic-photonic components such as lasers, modulators and detectors. However, frequency sweeps of radio-frequency (RF) photonic filters remain unwieldy due to the long simulation times of stepped frequency transient simulations. In this work, we present complex frequency chirp based methods for rapid frequency-domain simulation of PICs. The trade-offs involved in selecting the simulation parameters for a given frequency response accuracy and simulation time are studied along with the impact of windowing and frequency chirp profile. The presented method can result in over  $1000 \times$  improvement in simulation time of frequency sweeps of higher-order RF photonic filter topologies.

Index Terms—Optical filters, Photonic integrated circuits (PICs), RF Photonics, Silicon Photonics (SiP), Verilog-A.

#### I. INTRODUCTION

S ILICON-based electronic-photonic integration is a promising platform for pursuing advances in integrated circuits (IC) in the post-Moore's Law scaling era. As the complementary metal oxide semiconductor (CMOS) technology matures, IC advances are expected from the heterogeneous integration of novel devices such as the silicon-based photonics with standard Bi(CMOS). The large instantaneous bandwidth of integrated photonic devices allows enormous data transmission capacity reaching Terabits/s and the optical interconnects realized through on-chip and onboard waveguides and the optical fibers enable low-loss long-distance transmission at such speeds [1]. Silicon-oninsulator (SOI)-based photonics integrated circuits (PICs) are increasingly being used in data center interconnects to achieve higher data rates approaching 100Gbps/wavelength with reduced link energy consumption, compact size, and dramatically lower cost compared to discrete optics or III-V PICs [2]. The increased availability of multi-project wafer (MPW) services such as IME [3], IMEC [4], [5] and AIM

Md J. Shawon and V. Saxena are with the Department of Electrical and Computer Engineering, University of Delaware, Newark, DE, 19716 USA e-mail: shawon@udel.edu.

Photonics [6] are ushering in the Moore's Law equivalent of photonic ICs (where the number of components on a PIC double every two years [7]) by providing fabless PIC fabrication with a design flow similar to the standard CMOS electronic ICs as shown in Fig. 1). Furthermore, there is a growing interest in RF photonic ICs where the wide tunability and high selectivity of optical filters promise flexible RF front-ends [8], [9] and high dynamic range radio-on-fiber links for the next-generation wireless infrastructure [10], [11].

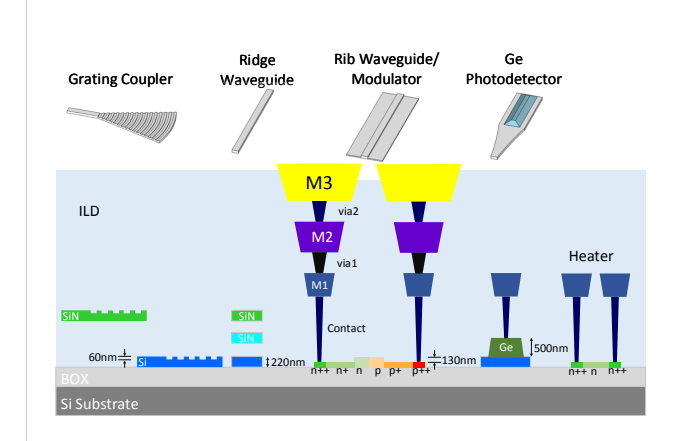


Fig. 1. Cross-section showing the layers in a typical silicon photonic fabrication process [2], [5], [12].

An ecosystem of design automation tools has recently emerged to support the growing demand for PIC design. However, these tools have taken a route where Finite-Difference Time-Domain (FDTD) numerical solvers for Maxwell's equations [13], [14] and mode solvers [15], [16] filled the short term need for device-level simulations. More recently, component and system-level simulators such as Lumerical's Interconnect [17] have emerged along with the wide selection of process design kits (PDKs) and simulation interfaces with electronic design automation (EDA) tools including Cadence Virtuoso and Mentor Graphics Pyxis. A major limitation of these simulators is that they idealize the electronics circuit blocks and their interaction with the photonic devices. For example, the bandwidth limitation is modeled by an ideal filter instead of capturing the nonlinear transient response when a modulator is driven by a transistor-level circuit. These limit the accuracy of hybrid electronic-photonic circuits especially at high speeds and fail to predict important artifacts. Thus, it is imperative for analog IC designers to entirely perform presilicon validation of photonic components along with circuits in an electronic EDA environment [18], [19].

The IC community has made progress with compact mod-

eling of photonic components using portable Verilog-A code [20], [21]. These compact photonic device models abstract but relevant optical as well as electrical characteristics for simulation using standard circuit simulators, such as Spectre [22]. It is expected that the compact models allow reasonably accurate estimation of frequency response as well as transient behavior with minimum simulation time and memory usage. Matrix transfer based methods have been employed with Lumerical Interconnect and Matlab to evaluate spectral response of photonic components [23], [24]. However, these models assume linearized steady-state device behavior and thus fail to accurately capture transient effects such as the photon lifetime in a ring modulator. Moreover, the specifics of analytic modeling technique for SOI waveguides, described later in Section II-C, necessitates time-domain (or transient) analysis

Current method of estimating spectral response of PICs employ stepped-frequency transient analysis (SFTA). In this method, the frequency is stepped in small increments, and for each frequency data point, a transient simulation is performed to obtain the steady-state magnitude and phase response of the PIC [23], [25], [26]. These simulations can be excruciatingly slow as the circuit simulator has to obtain steady-state transient response for each of the small frequency increments. Moreover for simulating PICs with higher frequency selectivity, the simulation time and accuracy trade-offs become unwieldy.

In this work, we describe a comprehensive approach to design and compact modeling of silicon PICs from the perspective of an electronic IC designer and present a rapid simulation method to determine frequency response by employing complex-valued frequency chirp stimulus. This article is organized as follows: Section II describes the photonic component modeling framework used in this work. In section III, we introduce a method for rapid simulation of frequency or wavelength domain response of photonic components that offer significant advantages over the previous methods. Trade-off between simulation time and accuracy are investigated and detailed to inform PIC designers. Section IV demonstrates CMOS photonic application circuits using experimental and simulation results, and presents the efficacy of our rapid simulation methodology followed by conclusion.

## II. PHOTONIC DESIGN FLOW AND COMPACT MODELING A. PIC Design Flow

In our PIC design flow, a primitive component cell is created with its Verilog-A model and layout view along with a symbol. A design rule check (DRC) clean layout is automatically generated using a parameterized Python script in KLayout [27] or Luceda IPKISS [15] environment. A library of these cells with their corresponding parametrized compact models are created for basic PIC building blocks, such as the waveguides, phase-shifters, couplers, splitter, combiners, lasers, etc., using simulations and experimental data from the foundry.

Complex PIC schematics and layout are created by hierarchically combining these constituent devices in the schematic and layout views. Top-level floorplan of the PIC is performed in the EDA tool (Cadence or Mentor Graphics), followed

by optical routing with low-loss bends using custom scripts [28]. Chip or block level DRCs are performed using Mentor's Calibre [29] using a foundry provided DRC rule deck. In the current art of the EDA integration for photonics, layout versus schematic (LVS) checks are available in Mentor Graphics Pyxis tool [30] using symbol level connectivity. However, automatic extraction of photonic devices from their layout, in a way similar to transistors, capacitors or resistors, is still unavailable. Although a fully automated design flow is still desired, the presented design flow has been successfully used to fabricate PICs by the authors as shown in Fig. 2.

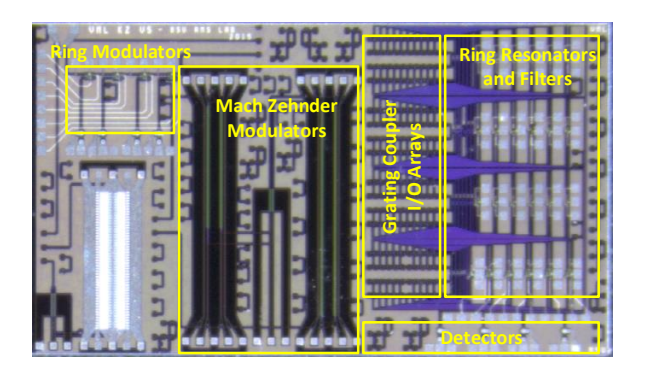


Fig. 2. Silicon Photonic Integrated Circuit (SiPIC) fabricated utilizing the PIC design flow and IME foundry through the CMC/SiEPIC program.

#### B. Baseband Equivalent Modeling

Silicon photonics operates in the mid- and long-wave infrared regions with telecommunications applications being concentrated around the 1330nm and 1550nm laser wavelengths. The latter wavelength translates into  $\omega_R=2\pi$ . 193 THz center frequency. However, since the signal is obtained by modulating the laser and limited by the electrical bandwidth of the photonic devices (typically <50GHz), only the bandpass spectrum around  $\omega_R$  is of interest. Thus, similar to carrier modulated communication systems, only the complex baseband equivalent signal and filter response are employed [23], [25]. Here,  $\tilde{E}(t)$  is the analytic field which is in turn related to the complex baseband field  $E_{bb}(t)$  by

$$\tilde{E}(t) = e^{j\omega_R t} E_{bb}(t) \tag{1}$$

Similar notations are developed for the baseband equivalent of the RF photonic filters:

$$\tilde{h}(t) = e^{j\omega_R t} h_{bb}(t); \quad \tilde{H}(j\omega) = H_{bb}(j(\omega - \omega_R))$$
 (2)

Here,  $h_{bb}(t)$  is the complex baseband equivalent impulse response of the optical filter, h(t), with respect to the laser carrier frequency.  $H_{bb}(j\omega)$  and  $H(j\omega)$  are their respective Fourier transforms [31]. Note that these are the baseband equivalent with respect to the laser frequency  $(\omega_R)$  and not any RF carrier frequency. The input output relationships are now given as [31]

$$E_{out,bb}(t) = \frac{1}{2}h_{bb}(t) * E_{in,bb}(t)$$
 (3)

Representing the optical signals and filters using their complex baseband significantly relaxes the transient time steps in simulation, i.e. from  $1\ fs$  to  $10\ ps$  range, which would otherwise be prohibitive to simulate. Also, from now onwards in this paper, only the baseband equivalent models are used and the subscript bb is dropped in the notations.

Since Verilog-A doesn't natively handle complex arithmetic, real and imaginary signals and filter coefficients are represented as an optical bus E[0:1]. The cartesian field is given by E[0]+jE[1] and polar by  $E[0]\angle(E[1])$ . Without loss of generality, we use electric field magnitude and phase as two Verilog-A 'natures' to represent light in an optical bus. To further simplify the modeling, we only model electric field in forward direction so the backscattering effect is ignored. Therefore, the directional blocks need to be carefully connected with each other. Also, cartesian to polar interconversion, addition and multiplication library blocks are utilized [23], [26].

#### C. Single-mode Waveguides

Single-mode waveguides are the fundamental building blocks in silicon-based PICs where foundry MPWs offer a single SOI and one or more silicon nitride routing levels as seen in Fig. 1. A ridge waveguide (essentially an optical equivalent of wire) is geometrically defined by its width while its height is fixed by the wafer or process (220nm for SOI), while a rib waveguide (used for creating pn junctions with metal contacts) has an additional etch level [1]. Silicon waveguides are dispersive, i.e. their effective index,  $n_e$  (a complex quantity) is wavelength (or frequency) dependent. In the compact model first-order dispersive effects are captured by the group index. Also, only the real part of  $n_e$  varies strongly with wavelength [32], [33] which is curve-fitted using the foundry provided data.

We have the wave vector given as

$$\beta(\lambda) = \frac{2\pi \cdot n(\lambda)}{\lambda} = \frac{\omega \cdot n(\omega)}{c} \tag{4}$$

where  $n \triangleq \Re(n_e)$  is the real part of the effective index. The wave vector can be expanded around the reference frequency,  $\omega_R$ , as [23], [25]

$$\beta(\omega) = \beta(\omega_R) + \frac{\partial \beta}{\partial \omega} \bigg|_{\omega_R} \Delta \omega + \dots = \beta(\omega_R) + \frac{n_g \Delta \omega}{c}$$
 (5)

where  $n_g$  is the group index:

$$n_g = n(\omega_R) + \frac{\omega_R}{c} \cdot \frac{dn}{d\omega}\Big|_{\omega_R} = n(\lambda_R) - \lambda_R \cdot \frac{dn}{d\lambda}\Big|_{\lambda_R}$$
 (6)

The imaginary component of  $n_e$  represents the waveguide loss and is approximated by a constant, i.e. the field-loss coefficient,  $\alpha_A = \Im(n_e)$ . The optical loss in a waveguide is typically expressed in dB/cm. The fields in the waveguide can be shown to be related by the following equation [23]

$$E_{out}(t) = e^{-\left(\alpha_A + j\beta(\omega_R)\right)L} \cdot E_{in}\left(t - \frac{n_g \cdot L}{c}\right) \tag{7}$$

where L is the waveguide length, and  $E_{in}(t)$  and  $E_{out}(t)$  are the input and output baseband equivalent electric fields.

In Eq. 7, the first product term represents initial phase at the reference frequency and the second term is the delay due to the group index,  $n_g$ . Eqn. 7 equation is implemented using the absdelay statement in Verilog-A as shown below:

```
module WG(in, out);
                  // in[0] + j*in[1]
input [0:1] in;
output [0:1] out;
opticalField [0:1] in, out;
//Convert the loss mag and phase into cartesian
Pol2Cart converter1(loss_pol, phi_pol, loss_cart);
//Lossy output without the group delay
CartMul cartMul1(loss_cart, in, out_nD);
analog begin
  // Field loss factor
  OptMag(loss_pol) <+ sqrt(loss_factor);
  // Initial phase
  OptPhase(phi_pol) <+ (-L*neff * 2*'PI/lambdaR)
    %(2* \PI);
  // Group delay
  OptE(out[0]) <+ absdelay(OptE(out_nD[0]),L*ng/'C);</pre>
  OptE(out[1]) <+ absdelay(OptE(out_nD[1]),L*ng/'C);</pre>
end //analog
endmodule
```

Listing 1. Key elements of the Verilog-A Waveguide model

The absdelay operator reflects the waveguide delay in a transient simulation but is replaced by a unity multiplier if Spectre 'ac' simulations are performed. Consequently, transient simulations are needed to determine the frequency response of the circuit at hand.

#### D. Continuous-wave Laser Source

In our model, reference wavelength (or frequency) of the continuous-wave (CW) laser is considered its "DC" operating point and the source generates monochromatic light at a frequency offset,  $\Delta\omega=2\pi\Delta f$ . In our baseband equivalent CW laser model, only the frequency offset is used as a sweep parameter which in turn influences the phase of the source electric field. Therefore, the laser electric field magnitude and phase can be expressed by the phasor [23], [26]:

$$E_{out} = E_{amp} \angle (\phi_0 + 2\pi \int_0^t \Delta f \cdot d\tau)$$
 (8)

Here,  $\phi_0$  is the initial phase.  $E_{amp}$  is set using a voltage source and  $E_{out}$  is evaluated by employing time integral operator in Verilog-A. Therefore, the CW laser source in simulations is a sinusoidally varying complex field at the offset frequency. Note that in Eq. 7, the group index is constant and thus the delay is also constant. However, since in the laser model the phase output is time integral of frequency offset, the constant delay results in different phase shifts at different frequency offsets.

#### E. Passive Photonic Building Blocks

1) Grating Coupler: Light is coupled between an optical fiber and the PIC either using a grating coupler (GC) or an edge coupler [1]. Grating couplers allow simplified chip testing and coupling to fiber arrays. GCs can be either single

polarization or polarization splitting type. The GC is designed for a coupling angle from the vertical plane, say  $8^\circ-22^\circ$  , and characterized by its loss profile [34]

$$Loss = -Loss_{peak} - \left(\frac{\lambda - \lambda_{peak}}{\lambda_{-3dB}/2\sqrt{3}}\right)^2 \tag{9}$$

with parameters peak loss ( $Loss_{peak}$ ), peak wavelength ( $\lambda_{peak}$ ), and 3dB bandwidth ( $\lambda_{-3dB}$ ). The typical measured loss in around 4-5 dB per coupling and depends upon the fiber tilt angle and spacing.

2) Waveguide Couplers: When two waveguides are brought in close proximity, the optical power is transferred back and forth between the waveguides along the direction of propagation. This is analyzed using coupled-mode theory and essentially realizes a directional coupler by appropriately sizing the coupling length and the gap [1]. In our unidirectional coupler model, the input and output are complex fields. The compact model allows wavelength independent (i.e. point coupler) as well as wavelength dependent coupling with associated delay and optical loss. Here,  $K_p = \kappa^2$  is the power coupling coefficient which is an input parameter to the model, where  $\kappa e^{-j\frac{\pi}{2}} = -j\kappa$  is the amount of field cross-coupling and  $t = \sqrt{1-\kappa_p}$  is the field through-coupling. For a lossless coupler, the field coupling coefficients satisfy the condition,  $\kappa^2 + t^2 = 1$ . With this notation, the resulting field coupling matrix is described as:

$$\begin{bmatrix} E_{o1} \\ E_{o2} \end{bmatrix} = \begin{bmatrix} t & -j\kappa \\ -j\kappa & t \end{bmatrix} \begin{bmatrix} E_{i1} \\ E_{i2} \end{bmatrix}$$
 (10)

In practice, the coupling matrix is wavelength dependent and the coupler loss includes the loss-dependent on the coupler length,  $L_c$ , and the bend loss. This data is either simulated using a mode solver or provided by the foundry.

3) Splitters and Combiners: Splitters and combiners are inverse of each other and are employed to build Mach Zehnder interferometric structures which find applications in optical modulators and filters. Y-branch and multi-mode interference (MMI) based splitters and couplers are available in the foundry PDKs. A  $2\times1$  MMI or Y-branch splits/combines optical power at  $k_s=0.5$  ratio [1] . The splitter compact model implements the following governing equation

$$\begin{bmatrix} E_{o1}(t) \\ E_{o2}(t) \end{bmatrix} = \begin{bmatrix} \sqrt{\alpha_s k_s} \\ \sqrt{\alpha_s (1 - k_s)} \end{bmatrix} E_{in}(t - t_d)$$
 (11)

where  $\alpha_s$  and  $t_d$  are the loss and delay, respectively.

#### F. Active Photonic Building Blocks

Active silicon photonics is build around the plasma or free carrier dispersion effect which at 1550 nm wavelength is described by the Soref and Bennett's equation [35]:

$$\Delta n(x,y) = -8.8 \times 10^{-22} \Delta N_e(x,y) - 8.5 \times 10^{-18} \Delta N_h^{0.8}(x,y)$$
$$\Delta \alpha(x,y) = 8.5 \times 10^{-18} \Delta N_e(x,y) + 6 \times 10^{-18} \Delta N_h(x,y)$$
(12)

Here,  $\Delta n(x,y)$  is the change in the real part of the effective index and  $\Delta \alpha(x,y)$  is the change in loss.  $\Delta N_e(x,y)$  and

 $\Delta N_h(x,y)$  are the spatial distribution of free electrons and holes respectively. The change in effective index,  $\Delta n(V)$ , and loss,  $\Delta \alpha(V)$ , as a function of voltage are obtained by numerically solving the overlap integral with the waveguide optical mode profile [36]. Optical phase shift can either be created thermally (due to thermal carrier generation) or electrically. The resultant phase shift for a phase shifter of length L at wavelength  $\lambda$  can be described by

$$\Delta\phi(V,\lambda) = \frac{2\pi L}{\lambda} \left( \Delta n(V) + \frac{dn}{dT} \cdot (T - T_0) \right)$$
 (13)

where  $\frac{dn}{dT} \approx 1.86 \times 10^{-4} K^{-1}$  is the thermo-optic coefficient for silicon and  $T_0 = 300 K$  [35].

1) Thermal Phase Shifters: Thermal phase shifters allow tuning of passive optical elements with a small footprint. Doped waveguides or tungsten resistors are employed for Joule heating of the waveguide sections. Since  $n_e$  is dependent upon temperature, which in turn depends upon the voltage (or current) applied across the heater, an optical phase shift is produced [12]. Since thermal modeling is computationally intensive, empirical curve-fitted models are used to relate the phase shift to the electrical stimulus. The I-V characteristics of the doped heater is given by [37], [38]

$$I = \frac{V}{R_0} \cdot \frac{2}{\sqrt{1 + K_v \cdot V}} \tag{14}$$

where  $R_0$  and  $K_v$  are fitted parameters. The optical phase shift as a function of the applied voltage,  $\Delta\phi(V)$ , is implemented in Verilog-A as a polynomial curve-fit.

- 2) High-speed Phase Modulators: High-speed phase modulators are constructed using the free carrier dispersion effect, which is realized using depletion-mode pn-junction or accumulation-mode metal-oxide-semiconductor (MOS) capacitor built around the rib waveguide. Intensity modulators are constructed from the phase modulators using either Mach Zehnder or microring modulator configuration that trade-off size, power and capacitance with robustness to process, voltage and temperature (PVT) variations [1]. The depletion-mode phase shifter is modeled using a polynomial fit of optical phase shift  $\Delta \phi(V)$ , loss  $\alpha(V)$ , and junction capacitance  $C_i(V)$  as function of applied voltage. Also, the finite electrical bandwidth is modeled using an RC network based on experimental data from the foundry. A detailed treatment of compact modeling active phase shifters is provided in literature (including authors' prior work) [18], [19], [39], [40].
- 3) Detector: Since silicon is transparent to infrared, germanium (Ge) waveguide photodetectors are included in the PIC MPW platforms [5], [6]. The compact model for photocurrent is described by

$$i_{pd} = I_{dark} + \frac{\rho \cdot |E_{in}|^2}{1 + s\tau} \tag{15}$$

where  $\rho$  is the responsitivity,  $I_{dark}$  is the dark current, and  $\tau$  is the optical response time-constant.

#### III. RAPID SIMULATION OF PHOTONIC COMPONENTS

When simulating Mach Zehnder modulators, the ability to perform transient simulations is sufficient to verify circuit functionality by just observing the eye diagrams [18], [19]. However, design of RF photonic filters requires frequency (or wavelength)-domain analysis. Therefore, to obtain the frequency response of a PIC, prior work employed SFTA simulations [23], [25]. SFTA method can be extremely slow, especially when the typical range of frequency sweep is 50 GHz or more to capture the Free Spectral Range (FSR) of ring resonators or filters. The frequency resolution should also be kept sufficiently high, so that the high-Q resonances of such components can be captured with reasonable accuracy. This necessitates simulation techniques for rapid frequency sweep without significant loss in accuracy.

#### A. Broadband Analytic Chirp Excitation

Instead of exciting the system with a frequency tone, a broadband source such as a frequency chirp can be applied to estimate its frequency response in a single transient simulation. A variety of chirps have been used in engineering disciplines to estimate frequency response of a wide range of systems with non-linear dynamics [41]–[44]. In our context, an analytic chirp signal is defined as

$$E_{ch}(t) = E_a(t) \cdot e^{j\varphi(t)} \tag{16}$$

In a strict definition, the amplitude evolution,  $E_a(t)$ , should be much slower than the phase oscillations,  $\varphi(t)$ , and is expressed by the conditions [45]

$$\epsilon_1 = \left| \frac{\dot{E}_a(t)}{E_a(t)\dot{\varphi}(t)} \right| \ll 1; \quad \epsilon_2 = \left| \frac{\ddot{\varphi}(t)}{\dot{\varphi}^2(t)} \right| \ll 1$$
(17)

For a simple chirp laser source,  $E_a(t) = E_{amp}$  is a constant field magnitude. The phase evolution depends upon the instantaneous frequency, which is swept from a start offset frequency,  $f_1$ , to the stop frequency,  $f_2$ , over the chirp duration, T, and is expressed as [44]

$$\varphi(t) = 2\pi \left( f_1 \cdot t + \frac{g \cdot t^{m+1}}{m+1} \right) \tag{18}$$

where g is a normalizing constant. For m=1, the output is a linear chirp and non-linear for m>1. The frequency can also evolve exponentially (i.e.  $f=f_1b^t$ ) or logarithmically (for hyperbolic chirps). For an exponential chirp,  $\varphi(t)=2\pi f_1(\frac{b^t-1}{\ln(b)})$ , where b is the exponential increase rate [46].

In our compact modeling environment, the laser source model in Eq. 8 is modified to include a chirped phase. The baseband equivalent linear chirp source is now given by

$$E_{out} = E_{amp} \angle \left(2\pi \int_0^t (f_1 + g \cdot \tau) d\tau\right)$$
 (19)

where  $g = \frac{f_2 - f_1}{T} = \frac{\Delta F}{T}$ ,  $\Delta F$  being the chirp bandwidth.

The baseband equivalent frequency response of the circuit or device under test (DUT) is estimated as

$$H[k] = \frac{X_{out}[k]}{X_{ch}[k]} \tag{20}$$

where  $X_{ch}$  are the  $N_{FFT}$ -point fast Fourier transform (FFT) of the complex input chirp and  $X_{out}$  is the FFT of the complex output of the DUT. Fig. 3 outlines the steps of estimating frequency response of a PIC using chirp signal. In order to satisfy the Nyquist sampling criterion for the entire chirp signal, a sampling rate of  $f_s \geq 2f_2$  is required.

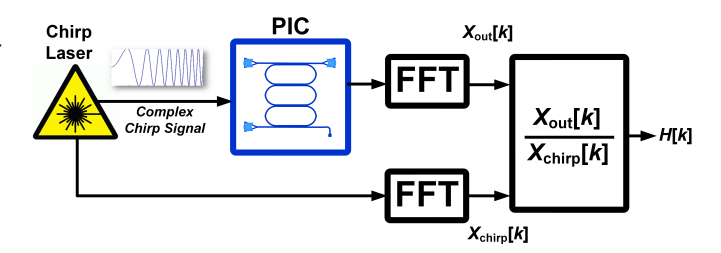


Fig. 3. Estimation of frequency response of PIC using our proposed analytic Frequency Chirp Method (FCM).

Fig. 4 illustrates the linear chirp from  $f_1=10\ GHz$  to  $f_2=60\ GHz$  with  $T=100\ ns$  generated using the Verilog-A source module. The spectrogram in Fig. 4 (top) shows a linear increase in frequency. Fig. 4 (bottom) illustrates the normalized FFT magnitude response of the complex chirp The chirp's FFT response exhibits ripples near the edges of desired frequency range (i.e. near  $f_1$  and  $f_2$ ). The ripples in the complex chirp source appear in the simulated PIC frequency response, H(k), leading to undesirable artifacts and inaccuracies and thus must be minimized.

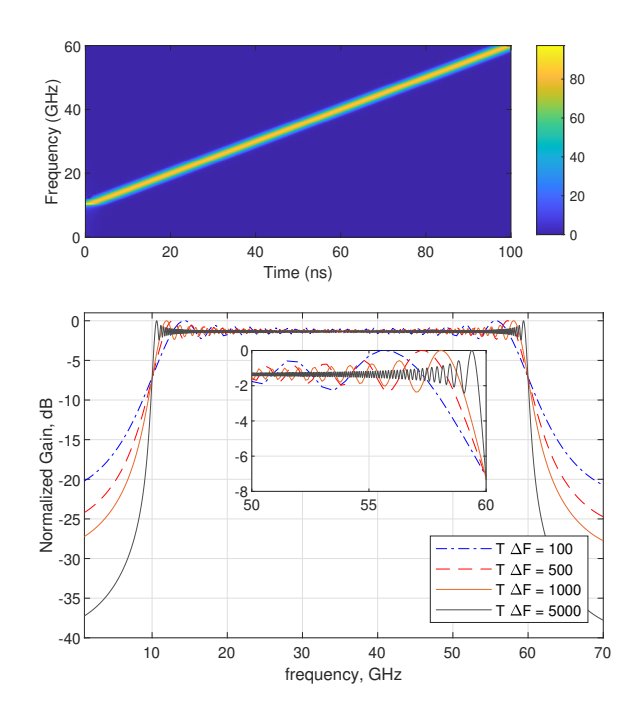


Fig. 4. (top) Spectrograph of a linear chirp source with  $\Delta F = 50 GHz$ , T = 100 ns. (bottom) Normalized FFT magnitude response of the analytic Chirp source with  $T\Delta F = 100, 500, 1000$ , and 5000. The inset shows the Fresnel ripples at the right edge of the spectrum (50 to 60 GHz).

#### B. Time-Bandwidth Product and Fresnel Ripples

In order to understand the source of ripples in the spectrum, Fourier integral of the chirp waveform is considered. Analytical expressions for the linear chirp, essentially a broadband frequency modulation (FM) signal, can be expressed in the form of Fresnel integrals [46], [47]:

$$|X_{ch}(f)| = \sqrt{\frac{T}{2\Delta F}} \left[ (C(x_1) + C(x_2))^2 + (S(x_1) + S(x_2))^2 \right]^{\frac{1}{2}}$$
(21)

$$\angle X_{ch}(f) = \tan^{-1}\left(\frac{S(x_1) + S(x_2)}{C(x_1) + C(x_2)}\right) - 2\pi(f - f_0)^2 \frac{T}{2\Delta F}$$
(22)

where,  $S(x) = \int_0^x sin(\frac{\pi y^2}{2}) dy$  and  $C(x) = \int_0^x cos(\frac{\pi y^2}{2}) dy$  are Fresnel integrals, and  $f_0 = \frac{f_1 + f_2}{2}$  is the center frequency. The Fresnel arguments  $x_1$  and  $x_2$  are given by

$$x_1 = \sqrt{\frac{T \cdot \Delta F}{2}} (1+r); \quad x_2 = \sqrt{\frac{T \cdot \Delta F}{2}} (1-r)$$
 (23)

where  $r=2(\frac{f-f_0}{\Delta F})$  is the scaled frequency. The first term in Eq. 22 approximates to a residual phase of  $\frac{\pi}{4}$  over a large frequency range of interest while the second term is the quadratic phase.

From Eqs. 21 - 23, the chirp spectra is a function of the time-bandwidth product,  $T \cdot \Delta F$ , and independent of center frequency and bandwidth. A lower value of time-bandwidth product results in larger Fresnel ripples in the magnitude spectrum [46]. As illustrated in Fig. 4 (bottom), with the increase in  $T \cdot \Delta F$  from 100 to 5000, the chirp magnitude spectrum gets closer to the ideal rectangular response with flat magnitude and the ripples get less pronounced in the frequency range of interest i.e. between  $f_1$  to  $f_2$ . Also, with a larger value of the  $T \cdot \Delta F$ , phase stays closer to  $\frac{\pi}{4}$  in the frequency range of interest [46], [47].

#### C. Simulation Parameter Selection

For rapid simulation of spectral response of the DUT, the time-bandwidth product plays a critical role. For lower ripple in the passband, a  $T \cdot \Delta F \geq 1000$  can be employed which effectively pushes the ripples to the edge of the spectrum. This sets the chirp length, T, for a given chirp bandwidth  $(\Delta F)$ . To illustrate the significance of  $T \cdot \Delta F$ , the spectral response of a ring resonator with a circumference of 8mm is shown in Fig. 5 for the input chirps seen in Fig. 4. Here, it is evident that a larger  $T \cdot \Delta F$  reduces Fresnel ripples in the frequency range of interest.

The duration of the analytic FCM transient simulation is set by the maximum time-step  $(t_{step})$  set by the Nyquist sampling rate, i.e.  $t_{step} \leq \frac{1}{2f_2}$ . However in practice, a sampling frequency of several multiples of the Nyquist rate is used to obtain the necessary FFT resolution,  $f_{res} = \frac{\Delta F}{N_{FFT}}$ , with  $N_{FFT} = \frac{T}{t_{step}}$ . Another less obvious consideration is the fact that the chirp excitation should be slower than the temporal dynamics of the DUT. This is particularly relevant for high-Q optical resonators where longer photon lifetime determines the

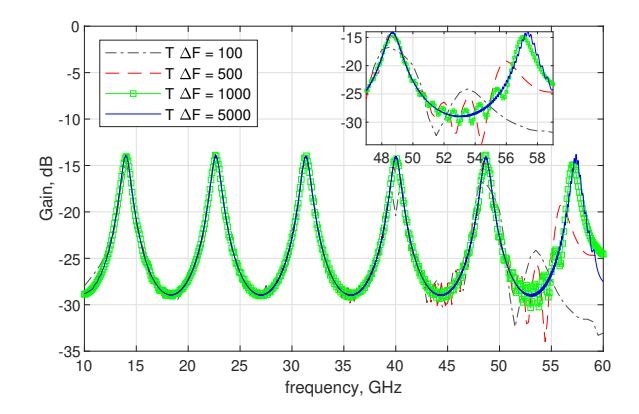


Fig. 5. Spectral response of a DUT (Ring Resonator) under  $T\Delta F=100,500,1000$  and 5000. The inset illustrates the DUT response at the edge of the Chirp spectrum (47 to 59 GHz) for better visualization.

settling time. Thus, the chirp rate should be much less than the circuit bandwidth, i.e.  $T \ge \frac{10}{f_{3dB}}$ ) and can be manually finetuned to improve simulation results. Due to this reason fast single-cycle chirps, known as the Titlets [44], are not suitable for frequency domain analysis.

Several categories of chirp profiles were introduced in Section III-A where the frequency changes in quadratic (m=2) or exponential fashion. Therefore, for the same sampling rate, the DUT will experience larger frequency steps as the chirp frequency approaches  $f_2$ . In this study, these non-linear chirps didn't provide any significant advantages over the linear chirps for the same simulation parameters.

#### D. Windowing

Based on the discussion in Sections III-B and III-C, the Fresnel ripples can be pushed to the edge of the desired spectrum by using a large time-bandwidth product. However, these ripples, seen in Fig. 5, still distort the magnitude spectrum at the edges. This is specially important in simulations where the full FSR for a filter is simulated and the filter passband is placed close to the frequency edges of the chirp excitation. As seen in Fig. 5, the spectral response of the drop port of the optical ring resonator suffers from the obtrusive Fresnel ripples near the passband edge. The impact of Fresnel ripples can be further mitigated by employing a suitable windowing function such as Tukey, Hann, Blackman-Harris, etc., in the time-domain. The idea is to retain the broadband spectral characteristics of the complex chirp while smoothening the temporal discontinuities at the edges. However, the condition in Eq. 17 should be satisfied where the relative change,  $\frac{E_a(t)}{E_a(t)}$ , in the output chirp amplitude should be small during a pseudoperiod  $\frac{2\pi}{|\dot{\phi}(t)|}$ , which again sets a limit on the chirp time, T.

The cosine-tapered function, better known as the Tukey window, is given by

$$X[n] = \begin{cases} \frac{1}{2}[1 + \cos(\pi(\frac{2n}{\alpha N} - 1))] & 0 \le n < \frac{\alpha N}{2} \\ 1 & \frac{\alpha N}{2} \le n \le N(1 - \frac{\alpha}{2}) \\ \frac{1}{2}[1 + \cos(\pi(\frac{2n}{\alpha N} - \frac{2}{\alpha} + 1))] & N(1 - \frac{\alpha}{2}) < n \le N \end{cases}$$
(24)

where, N and  $\alpha$  are the total number of samples and cosine factor, respectively. A representative Verilog-A code

description of the chirp laser with Tukey window is shown in Listing 2.

```
module Laser_Chirp_Tukey(out, Vin);
electrical Vin:
output [0:1] out;
opticalField [0:1] out; // E = E[0] + j*E[1]
//Internal nodes
opticalMag outMag;
opticalPhase outPhase;
analog begin
  @(initial_step) begin
    frate = (f2-f1)/Tsw;
  // Amplitude
  freq = f1 + frate*$abstime;
  if ($abstime < Tsw*alpha/2) begin</pre>
    OptMag(outMag) <+ V(Vin) * 0.5*(1+cos('PI*((2*
    $abstime/(alpha*Tsw))-1)));
  end else if (($abstime >= Tsw*alpha/2) &&
    $abstime<=(Tsw-(Tsw*alpha/2)))) begin</pre>
    OptMag(outMag) <+ V(Vin);
  end else begin
    OptMag(outMag) <+ V(Vin) *0.5*(1+cos('PI*('2*
    abstime/(alpha*Tsw))-(2/alpha)+1)));
  OptPhase(outPhase) <+ idt(2*'PI*(f1+ frate*
    $abstime),0);
end //analog
Pol2Cart out_conv(outMag, outPhase, out);
```

Listing 2. Sections of complex chirp source model with Tukey window.

Fig. 6 presents comparison of spectrum of linear chirp laser modified with Rectangular, Hanning, and Tukey window functions and their effectiveness in suppressing ripples. The chirp laser with non-rectangular window functions lead to excellent ripple suppression, even with very low time-bandwidth product. Excellent ripple suppression can easily be obtained with  $T \cdot \Delta F$  as low as 50. Due to the significant reduction in ripples, smoothly varying windows are the best candidates for optical filters with high-Q resonant structures. Thus, the subsequent simulations in this study are performed complex chirp stimulus with Tukey window and with  $\alpha = 0.3$  cosine factor. Its important to note the flat amplitude spectrum of the complex chirp signal is not necessary since the output spectrum will be normalized by the input chirp spectrum to obtain the frequency response.

#### IV. RF PHOTONIC APPLICATION CIRCUITS

Spectral response of several photonic application circuits have been simulated and verified with an industry standard PIC simulator and with experimental measurements. The simulations were performed using Cadence Virtuoso IC6.1.7 running on CentOS Linux 6.9 on a Dell PowerEdge R440 Server with Dual Intel Xeon Silver 4214 CPUs operating at 2.2GHz and 16GB DRAM.

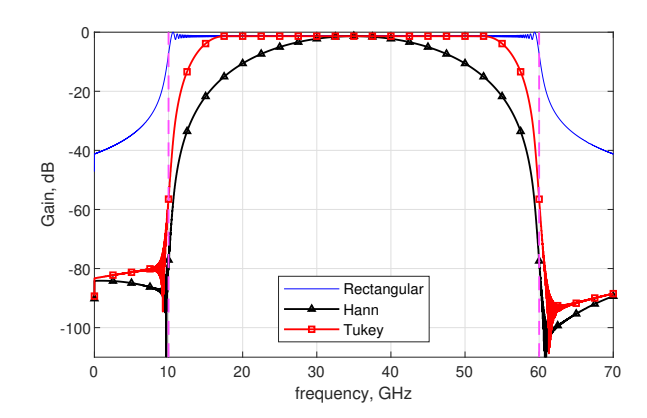


Fig. 6. Normalized FFT magnitude response of linear chirp source windowed with Rectangular, Hanning and Tukey functions. Here, the linear chirp source  $\Delta F = 50 GHz$ .

#### A. CROW Filter

Coupled Resonator Optical Waveguide (CROW) filters are widely used in wavelength division multiplexing (WDM) and Amplified Spontaneous Emission (ASE) filters [48]. As the name suggests, CROW filters are realized by coupling bus waveguides with multiple cascaded optical cavities (microrings) as shown in Fig. 7. In this study, a CROW filter of third order was designed and simulated with the design parameters summarized in Table I.

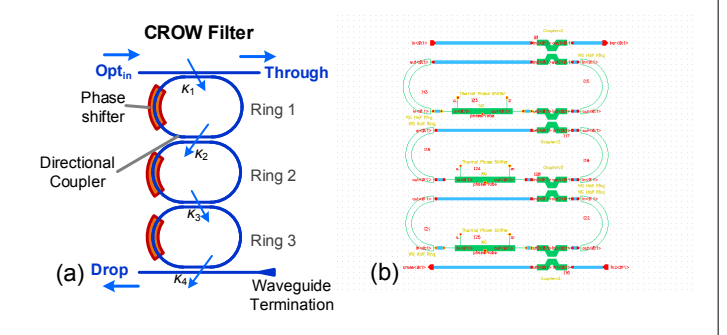


Fig. 7. (a) Third-order CROW filter topology, (b) Cadence schematic of the CROW.

### TABLE I CROW FILTER DESIGN PARAMETERS

Design Parameter	Value		
Ring Circumference (all 3)	500 μm		
Coupling coefficients: $[\kappa_1 \kappa_2 \kappa_3 \kappa_4]$	[0.1 0.08 0.08 0.1]		

This CROW filter is then simulated in our compact modeling framework and analytic FCM. The same filter is also simulated in Lumerical Interconnect - an industry standard photonic integrated circuit simulation tool [17] and with a foundry PDK from IMEC [5]. Excellent match between the two spectral responses, evaluated in two different simulation platforms, is observed (as shown in Fig. 8). This confirms the accuracy of the compact Verilog-A models of our photonic library components. The same CROW filter is also simulated

in Cadence Virtuoso platform employing the SFTA method and the results are compared in Table III.

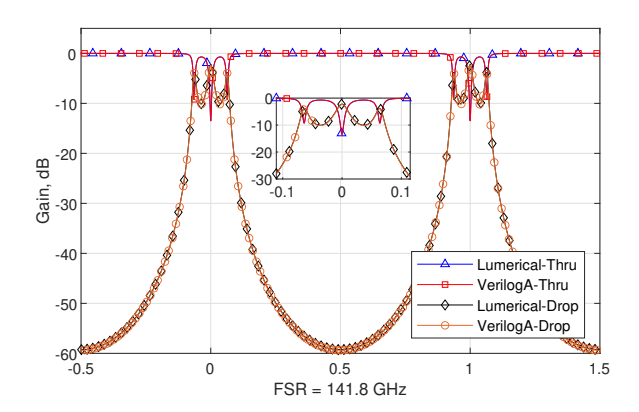


Fig. 8. Estimation of Spectral response of a CROW filter utilizing Lumerical Interconnect and analytic FCM. Here, linear chirp source  $\Delta F=400 {\rm GHz}$  and FSR = 141.8GHz.

The spectral response estimation with a frequency resolution of 1 GHz took 205s to execute using SFTA. In comparison, analytic FCM with  $T \cdot \Delta F = 2000$  took only 3.23s for the same frequency resolution and accuracy, which resulted in a  $63 \times$  improvement.

#### B. APF-based Higher-Order Filters

To further evaluate of our method, a PIC with much higher level of complexity is demonstrated. As shown in Fig. 9, All-Pass-Filter (APF) based optical filter is implemented using ring resonators coupled with the arms of a Mach Zehnder interferometer. To design the filter, all pass decomposition method described in [49] is employed that synthesizes a discrete-time Infinite Impulse Response (IIR) into an analog passive ring based structure. First, the filter specifications are translated to a Chebyshev Type-II IIR filter characteristic polynomial. Afterwards, the all pass decomposition method is employed to estimate the analog optical filter design parameters, i.e. the coupling coefficients  $(\kappa_j)$ , and phase shifts  $(\beta$  and  $\phi_j)$  [24], [50], [51]. A sixth-order APF-based filter specifications and design parameters are summarised in Table II.

 $\label{thm:constraints} \textbf{TABLE II} \\ \textbf{APF-based Filter Specifications and Design Parameters} \\$ 

APF-based Filter Specifications	Value
Filter Order	6
Bandwidth, BW	2 GHz
Stopband Attenuation	60 dB
Stopband Edge Frequency	$f_c\pm 2~\mathrm{GHz}$
Design Parameter	Value
Ring Circumference (all 6)	500 μm
Coupling coefficients: $[\kappa_1 \kappa_2 \kappa_3]$	[0.0712 0.3066 0.2056]
Mach Zehnder Arm Phase Shift, $\beta$	-1.5723 rad
$[\phi_1  \phi_2  \phi_3]$	[0.1624 0.0579 -0.1356] rad

The spectral response of the filter is then estimated using both Lumerical Interconnect and our simulation framework, utilizing SiP foundry provided data. Again, an excellent match

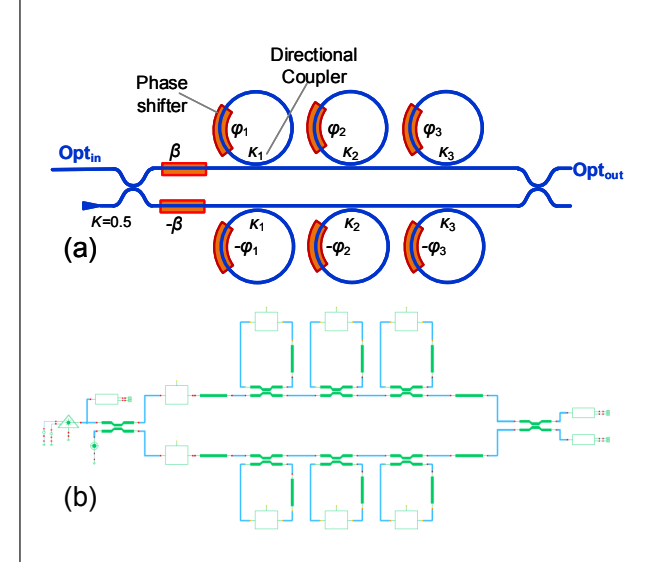


Fig. 9. (a) Topology of a sixth-order APF-based filter (b) Cadence schematic of the APF-based Filter.

between the two spectral responses is observed in Fig. 10. The analytic FCM method, with  $T \cdot \Delta F = 1600$ , took 7.21s to estimate the spectral response compared to 1499.1s taken by SFTA, resulting in  $208 \times$  speed up in simulation time.

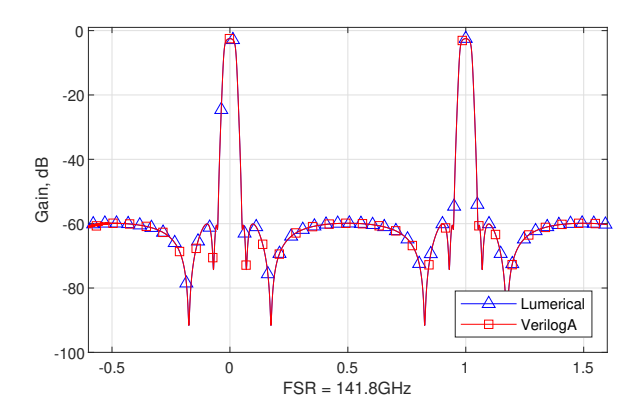


Fig. 10. Estimation of Spectral response of a sixth-order APF-based filter utilizing Lumerical Interconnect and analytic FCM. Here, the linear chirp source  $\Delta F=320 {\rm GHz}$  and FSR = 141.8GHz

#### C. Fabricated Dual-Bus Ring Resonator

Here, several PIC components were studied and fabricated (refer to Fig. 11) using IME's SiP MPW foundry with 248nm DUV lithography [52]. The components selected for this study are a Dual-Bus Ring Resonator (DUT 1) and Vernier Rings (DUT 2) as shown in Fig. 11.

The PIC characterization process involves coupling light from a tunable laser source (Keysight 81940A) into the SOI waveguide via on-chip grating couplers. The through and drop port optical signals of the PICs are then coupled into a single-mode polarization maintaining fiber (PMF) array through on-chip grating couplers at  $127\mu m$  pitch and terminated at a high-speed optical detector (Keysight N7744A). The spectral responses of the PICs are then obtained by sweeping the laser wavelength.

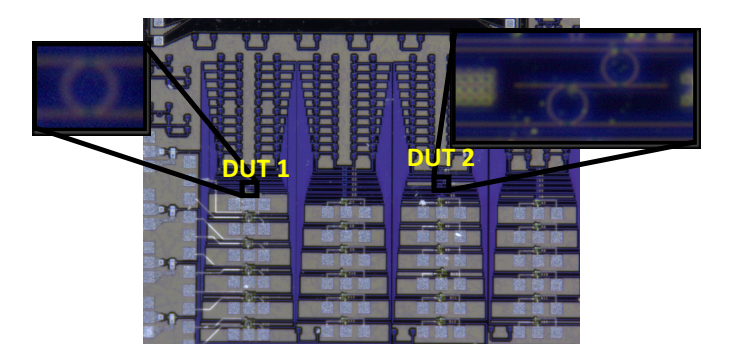


Fig. 11. Fabricated Photonic Chip using IME Silicon Photonic process. It contains several microring-based photonic filters including ring resonator (DUT 1) and Vernier Ring filter (DUT 2).

The fabricated dual bus ring resonator shown in Fig. 11 has a radius of 6.786  $\mu m$  and ring-to-bus gap of 200nm. The measured and simulated (using FCM) spectral responses are presented in Fig. 12. Again, excellent match is observed between the measured and FCM simulation. The slight inconsistency can be attributed to fabrication variation and ring losses. It is important to note that the grating coupler and optical routing loss has been de-embedded from the measured ring response. For this ring resonator, SFTA simulation took 1552s to estimate the response with a frequency resolution of 1 GHz while our FCM (with  $T \cdot \Delta F = 11000$ ) was significantly faster (11.44s) for the same level of accuracy.

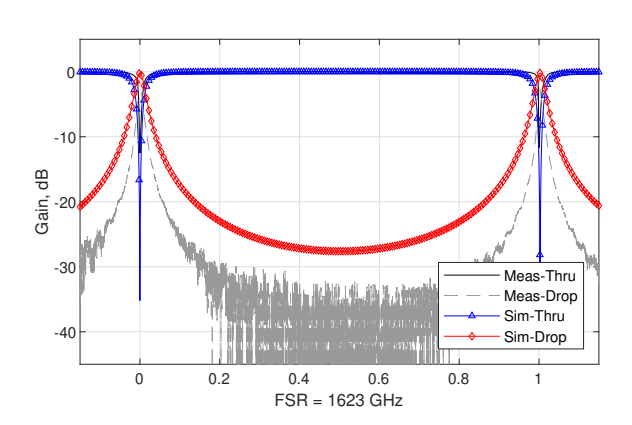


Fig. 12. Spectral response of the fabricated ring resonator. Here,  $\Delta F=2.2 {
m THz}$  and FSR = 1.6232 THz

#### D. Fabricated Vernier Ring Filter

The fabricated Vernier Ring filter (DUT2) shown in Fig. 11 consists of two rings coupled through a bus (middle) and two outer buses facilitating through and drop ports. The radius of the two rings are 10 and 11  $\mu$ m. Each ring is separated from the busses by 200 nm. Moreover, the middle bus is optically terminated in order to reduce reflections. Again, the measured result, presented in Fig. 13, confirms the FCM simulation, validating the accuracy of our Frequency Chirp Method. Furthermore, for this vernier ring, the time required to estimate spectral response with the same level of accuracy and a frequency resolution of 1 GHz using SFTA and FCM (with  $T \cdot \Delta F = 11000$ ) was 8350s and 20.8s, respectively.

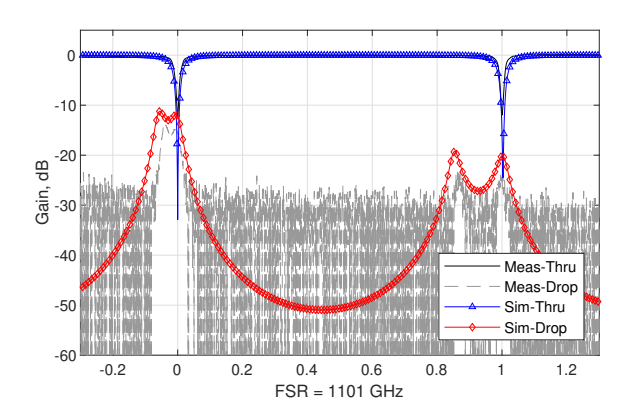


Fig. 13. Spectral response of the fabricated Vernier Ring filter. Here, the linear chirp source  $\Delta F=2.2 {
m THz}$  and FSR = 1.1012THz

#### E. Performance Summary

Here, we compare the simulation accuracy of the SFTA method with our analytic FCM method which is summarized in Table III. In order to allow a fair comparison, we compare the simulation time for each design, for the same frequency resolution ( $f_{res}$ ) and simulation accuracy. The simulation accuracy is defined using the Mean-Squared Error (MSE) of the filter magnitude response in dB, compared against a baseline simulation. The MSE is calculated as

$$MSE = \frac{1}{N_s} \sum_{k=0}^{N_s - 1} (|X[k]|_{dB} - |X_{baseline}[k]|_{dB})^2$$
 (25)

where,  $N_s$  is the number of frequency points,  $|X|_{dB}$  and  $|X_{baseline}|_{dB}$  are the filter magnitude response, in dB, for the relaxed and baseline simulation settings (described later), respectively. In Table III, MSEs were selected based on the filter selectivity, i.e. lower MSE for sharper filter response with respect to the FSR.

TABLE III PERFORMANCE COMPARISON

Design	$\Delta F$	$f_{res}$	SFTA	FCM	MSE	Improv.
CROW	400GHz	1GHz	205s	3.23s	0.12	63×
APF6	320GHz	1GHz	1499.1s	7.21s	0.46	208×
APF6	320GHz	0.1GHz	17215s	17.06s	0.13	1009×
Ring	2.2THz	1GHz	1552s	11.44s	0.015	135×
Vernier	2.2THz	1GHz	8350s	20.84s	0.06	400×

As observed in Table III, the proposed analytic FCM method took significantly less time, compared to SFTA, to estimate the spectral response of the PICs for the same accuracy and frequency resolution. This proposed method becomes even more advantageous when spectral estimation with high frequency resolution,  $f_{res}$ , is required. For example, for the APF-based optical filter, a  $10\times$  increase in resolution from 1 to 0.1 GHz results in  $4.85\times$  performance improvement factor (i.e. from  $208\times$  to  $1009\times$ ) with FCM. Moreover, when the frequency range of interest ( $\Delta F$ ) is very wide (e.g. for the

ring and vernier filters in Table III), our method offers orders of magnitude improvement in computation time.

Table IV compares the performance of analytic FCM with SFTA for the sixth-order optical filter, as the user relaxes the SFTA transient stop-time  $(t_{stop})$  and simulation time-step  $(t_{step})$  settings for a given frequency-offset step (or the corresponding time-period,  $T_p$ ). In order to maximize the efficiency of SFTA, we employ global SFTA sweep parameters: number of time periods  $N_1 = \frac{t_{stop}}{T_p}$ , and number of time-steps per time-period  $N_2 = \frac{T_p}{t_{step}}$ . Thus, for each frequency-offset, only the necessary  $t_{step}$  and  $t_{stop}$  are employed to achieve the desired accuracy and unnecessary data points are not computed and collected. This will result in an efficient SFTA, thus enabling a fair comparison with analytic FCM. The baseline simulation was performed using the conventional SFTA with a very long simulation time, i.e.  $N_1 = 1500$ , and small sampling time-step, i.e.  $N_2 = 100$ . As illustrated in Fig. 14 as  $N_1$  and  $N_2$  are relaxed, the MSE increases drastically while the simulation time is reduced. Thus, if SFTA is relaxed to reduce the simulation speed up gap with FCM, the simulation accuracy is sacrificed. For example, in Table IV, for the same MSE = 0.46 and frequency resolution, FCM still offers a 208× simulation time improvement over heavily optimized SFTA.

TABLE IV

COMPARISON OF PERFORMANCE FOR VARYING SFTA SETTINGS FOR THE SIXTH-ORDER OPTICAL FILTER (APF-6).

SFTA Settings	$N_1 = \frac{t_{stop}}{T_p}$	$N_2 = \frac{T_p}{t_{step}}$	Sim. Time	MSE
Baseline	1500	100	> 4hrs	0
A	10	100	220s	531.18
В	50	100	658s	488.71
С	245	100	2959.2s	0.88
D	245	20	802.8s	4.37
Е	245	5	280s	42.68
F	248	50	1499.1s	0.46
FCM	$T \cdot \Delta F = 1600$		7.21s	0.46

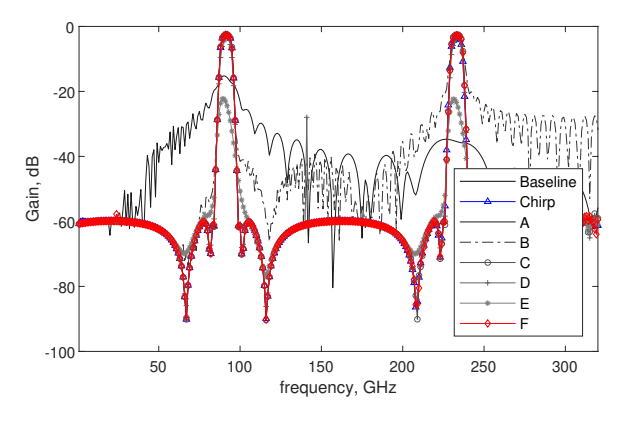


Fig. 14. SFTA performance, and its comparison with baseline and FCM results, as the stop-time and time-step parameters  $N_1$  and  $N_2$  are relaxed as per the settings A-F in Table IV.

#### V. CONCLUSION

In this work, a compact modeling and simulation framework for PICs using standard CMOS IC design tools is presented. A rapid simulation methodology has been proposed using analytic chirp waveforms for simulating frequency response of PICs. A combination of moderate time-bandwidth product and windowing schemes allows faster simulation while mitigating the ripple artifacts in the simulated PIC spectrum. This methodology is employed to estimate spectral response of APF-based and CROW filters, and up to  $1000 \times$  improvement was observed in execution time of the simulation. Lastly, the presented analytic FCM method will allow orders of magnitude improvement in time taken to perform Monte Carlo analysis of PICs. The Verilog-A models can be easily extended to include the process statistical variation data from the silicon photonic foundries for Monte Carlo analysis.

#### ACKNOWLEDGMENT

This work was supported by the Air Force Office of Sponsored Research (AFOSR) YIP Award under Grant FA9550-17-1-0076, NSF CAREER Award under Grant EECS-1454411, and Keysight Innovation Research Program. We would also like to thank Prof. Lukas Chrostowski and SiEPIC program for chip fabrication.

#### REFERENCES

- L. Chrostowski and M. Hochberg, Silicon Photonics Design: From Devices to Systems. Cambridge University Press, 2015.
- [2] M. Hochberg, N. C. Harris, R. Ding, Y. Zhang, A. Novack, Z. Xuan, and T. Baehr-Jones, "silicon Photonics: The Next Fabless Semiconductor Industry," *IEEE Solid-State Circuits Magazine*, vol. 5, no. 1, pp. 48–58, 2013.
- [3] T. Baehr-Jones, R. Ding, A. Ayazi, T. Pinguet, M. Streshinsky, N. Harris, J. Li, L. He, M. Gould, Y. Zhang, A. Eu-Jin, T.-Y. Liow, S. Hwee-Gee, G.-Q.-Q. Lo, and M. Hochberg, "A 25 Gb/s Silicon Photonics Platform," arXiv preprint arXiv:1203.0767, 2012. [Online]. Available: http://arxiv.org/abs/1203.0767
- [4] P. Dumon, W. Bogaerts, R. Baets, J.-M. Fedeli, and L. Fulbert, "Towards foundry approach for silicon photonics: silicon photonics platform ePIXfab," *Electronics letters*, vol. 45, no. 12, pp. 581–582, 2009.
- [5] "IMEC Silicon Photonics iSiPP50G." [Online]. Available: http://europractice-ic.com/mpw-prototyping/siphotonics/imec/
- [6] "AIM Photonics Process Design Kits (PDKs)." [Online]. Available: http://www.aimphotonics.com/pdk/
- [7] A. Khanna, Y. Chen, A. Novack, Y. Liu, R. Ding, T. Baehr-Jones, and M. Hochberg, "Complexity scaling in silicon photonics," in *Optical Fiber Communication Conference*. Optical Society of America, 2017, pp. Th1B–3.
- [8] G. Choo, S. Cai, B. Wang, C. K. Madsen, K. Entesari, and S. Palermo, "Automatic monitor-based tuning of reconfigurable silicon photonic apf-based pole/zero filters," *Journal of Lightwave Technology*, vol. 36, no. 10, pp. 1899–1911, 2018.
- [9] J. Shawon, Md., R. Wang, and V. Saxena, "Design and Modeling of Silicon Photonic Ring-Based Linearized RF-to-Optical Modulator," in in the proceedings of IEEE Int. Midwest Symposium on Circuits and Systems (MWSCAS), 2018.
- [10] A. Jain, N. Hosseinzadeh, X. Wu, H. K. Tsang, R. Helkey, J. E. Bowers, and J. F. Buckwalter, "A high spur-free dynamic range silicon dc kerr ring modulator for rf applications," *Journal of Lightwave Technology*, vol. 37, no. 13, pp. 3261–3272, 2019.
- [11] R. Helkey, A. A. Saleh, J. Buckwalter, and J. E. Bowers, "High-performance photonic integrated circuits on silicon," *IEEE Journal of Selected Topics in Quantum Electronics*, vol. 25, no. 5, pp. 1–15, 2019.
- [12] "Integrated Photonics Process Design Kit (PDK)," Online, Jul. 2018. [Online]. Available: http://www.aimphotonics.com/pdk/

- [13] A. F. Oskooi, D. Roundy, M. Ibanescu, P. Bermel, J. D. Joannopoulos, and S. G. Johnson, "MEEP: A flexible free-software package for electromagnetic simulations by the FDTD method," *Computer Physics Communications*, vol. 181, no. 3, pp. 687–702, 2010.
- [14] FDTD Solutions 8.9, Lumerical Inc. [Online]. Available: https://www.lumerical.com/tcad-products/fdtd/
- [15] W. Bogaerts and P. Dumon, "IPKISS Design Framework." [Online]. Available: http://www.ipkiss.org/
- [16] DEVICE 4.1, Lumerical Inc. [Online]. Available: https://www.lumerical. com/tcad-products/device/
- [17] INTERCONNECT 4.1, Lumerical Inc. [Online]. Available: https://www.lumerical.com/tcad-products/interconnect/
- [18] K. Zhu, V. Saxena, and W. Kuang, "Compact Verilog-A Modeling of Silicon Traveling-Wave Modulator for Hybrid CMOS Photonic Circuit Design," in 57th IEEE International Midwest Symposium on Circuits and Systems (MWSCAS), Aug 2014.
- [19] K. Zhu, V. Saxena, X. Wu, and W. Kuang, "Design Considerations for Traveling-Wave Modulator-Based CMOS Photonic Transmitters," *IEEE Transactions on Circuits and Systems II: Express Briefs*, vol. 62, no. 4, pp. 412–416, April 2015.
- [20] K. Kundert and O. Zinke, The Designer's Guide to Verilog-AMS. Springer, 2004.
- [21] C. C. McAndrew, G. J. Coram, K. K. Gullapalli, J. R. Jones, L. W. Nagel, A. S. Roy, J. Roychowdhury, A. J. Scholten, G. D. Smit, X. Wang et al., "Best practices for compact modeling in verilog-a," *IEEE Journal of the Electron Devices Society*, vol. 3, no. 5, pp. 383–396, 2015.
- [22] SpectreRF User Guide, Cadence Design Systems, 2003. [Online]. Available: https://www.cadence.com
- [23] C. Sorace-Agaskar, J. Leu, M. R. Watts, and V. Stojanovic, "Electro-optical co-simulation for integrated cmos photonic circuits with veriloga," *Optics express*, vol. 23, no. 21, pp. 27180–27203, 2015.
- [24] G. Choo, S. Cai, B. Wang, C. K. Madsen, K. Entesari, and S. Palermo, "Automatic monitor-based tuning of reconfigurable silicon photonic apf-based pole/zero filters," *Journal of Lightwave Technology*, vol. 36, no. 10, pp. 1899–1911, 2018.
- [25] C. M. Sorace-Agaskar, "Analog integrated photonics," Ph.D. dissertation, Massachusetts Institute Of Technology, 2015.
- [26] E. Kononov, "Modeling photonic links in verilog-a," Ph.D. dissertation, Massachusetts Institute of Technology, 2013.
- [27] L. Chrostowski, Z. Lu, J. Flueckiger, X. Wang, J. Klein, A. Liu, J. Jhoja, and J. Pond, "Design and simulation of silicon photonic schematics and layouts," in *Silicon Photonics and Photonic Integrated Circuits V*, vol. 9891. International Society for Optics and Photonics, 2016, p. 989114.
- [28] L. Chrostowski, J. Flueckiger, C. Lin, M. Hochberg, J. Pond, J. Klein, J. Ferguson, and C. Cone, "Design methodologies for silicon photonic integrated circuits," in SPIE OPTO, 2014, p. 89890G.
- [29] M. G. Calibre, "Mentor graphics." [Online]. Available: https://www.mentor.com/products/ic\_nanometer\_design/ verification-signoff/physical-verification/
- [30] M. G. Pyxis, "Mentor graphics." [Online]. Available: https://www.mentor.com/products/ic\_nanometer\_design/ custom-ic-design/pyxis-layout/
- [31] J. Cioffi, Signal Processing and Detection. Stanford University. [Online]. Available: https://web.stanford.edu/group/cioffi/doc/book/
- [32] M. J. Shawon, R. Wang, and V. Saxena, "Design and modeling of silicon photonic ring-based linearized rf-to-optical modulator," in 2018 IEEE 61st International Midwest Symposium on Circuits and Systems (MWSCAS), Aug 2018, pp. 348–351.
- [33] R. Wang, M. J. Shawon, and V. Saxena, "Design and compact modeling of silicon-photonic coupling-based ring modulators for optical interconnects," in 2018 IEEE 61st International Midwest Symposium on Circuits and Systems (MWSCAS), Aug 2018, pp. 619–622.
- [34] K. Zhu, "Integrated Circuit Design for Hybrid Optoelectronic Interconnects," Ph.D. dissertation, Boise State University, 2016.
- [35] R. A. Soref and B. R. Bennett, "Electrooptical effects in silicon," *IEEE Journal of Quantum Electronics*, vol. 23, no. 1, pp. 123–129, 1987.
- [36] H. Kogelnik, "Theory of optical waveguides," in *Guided-wave optoelectronics*. Springer, 1988, pp. 7–88.
- [37] M. Bahadori, A. Gazman, N. Janosik, S. Rumley, Z. Zhu, R. Polster, Q. Cheng, and K. Bergman, "Thermal rectification of integrated microheaters for microring resonators in silicon photonics platform," *Journal* of Lightwave Technology, vol. 36, no. 3, pp. 773–788, 2017.
- [38] A. Gazman, E. Manzhosov, C. Browning, M. Bahadori, Y. London, L. Barry, and K. Bergman, "Tapless and topology agnostic calibration solution for silicon photonic switches," *Optics express*, vol. 26, no. 25, pp. 32 662–32 674, 2018.

- [39] K. Zhu, C. Li, N. Qi, K. Yu, M. Fiorentino, R. Beausoleil, and V. Saxena, "Modeling of MZM-based Photonic Link Power Budget," in *IEEE Optical Interconnects Conference (OI)*, 2016. IEEE, 2016, pp. 58–59
- [40] Z. Kehan, V. Saxena, and X. Wu, "A Comprehensive Design Approach for a MZM Based PAM-4 Silicon Photonic Transmitter," in *International Midwest Symposium on Circuits and System (MWSCAS)*, Fort Collins, USA, Aug 2015.
- [41] X.-G. Xia, "System identification using chirp signals and time-variant filters in the joint time-frequency domain," *IEEE Transactions on Signal Processing*, vol. 45, no. 8, pp. 2072–2084, 1997.
- [42] S. Qian and D. Chen, "Joint time-frequency analysis," *IEEE Signal Processing Magazine*, vol. 16, no. 2, pp. 52–67, 1999.
- [43] I. H. Chan, "Swept sine chirps for measuring impulse response [j]," Power (dBVrms), vol. 50, no. 40, p. 30, 2010.
- [44] T. Paavle, M. Min, and T. Parve, "Aspects of using chirp excitation for estimation of bioimpedance spectrum," in *Fourier Transform-Signal Processing*. IntechOpen, 2012.
- [45] P. Flandrin, "Time frequency and chirps," in Wavelet Applications VIII, vol. 4391. International Society for Optics and Photonics, 2001, pp. 161–175.
- [46] C. Cook and M. Bernfeld, Radar Signals: An Introduction to Theory and Application. Academic Press, 1967.
  [47] "Chirp spectrum." [Online]. Available: https://web.archive.org/web/
- [47] "Chirp spectrum." [Online]. Available: https://web.archive.org/web/ 20191111030920/https://en.wikipedia.org/wiki/Chirp\_spectrum
- [48] S. Romero-García, A. Moscoso-Mártir, J. Müller, B. Shen, F. Merget, and J. Witzens, "Wideband multi-stage crow filters with relaxed fabrication tolerances," *Optics express*, vol. 26, no. 4, pp. 4723–4737, 2018.
- [49] P. A. Regalia, S. K. Mitra, and P. Vaidyanathan, "The digital all-pass filter: A versatile signal processing building block," *Proceedings of the IEEE*, vol. 76, no. 1, pp. 19–37, 1988.
- [50] C. Madsen, "Efficient architectures for exactly realizing optical filters with optimum bandpass designs," *Photonics Technology Letters, IEEE*, vol. 10, no. 8, pp. 1136–1138, 1998.
- [51] C. K. Madsen and J. H. Zhao, Optical Filter Design and Analysis. Wiley-Interscience, 1999.
- [52] "IME Photonics Multiple Project Wafer (MPW) Prototyping Service." [Online]. Available: https://www.a-star.edu.sg/ime/RESEARCH/ NANO-PHOTONICS-PROGRAMME/photonics\_multiple\_project\_ wafer\_mpw\_prototyping.aspx



Md Jubayer Shawon is pursuing his Doctoral degree in Electrical and Computer Engineering at the University of Delaware, DE. His research includes design of large-scale RF photonic integrated circuits that combine CMOS and Silicon Photonic ICs, and enable ultra-wide bandwidth and rapid reconfiguration of wireless transceivers over RF and millimeterwave frequency bands. He has also worked on CMOS RF MEMS devices with the Technology Development group of SilTerra, Malaysia. Additionally, in 2016, he worked at IMEC, Belgium in developing

control electronics for Smart Photovoltaic arrays. He has co-authored in several international journals and conference proceedings including IEEE Photonic Journal, European Physics Journal Plus, IEEE International Midwest Symposium on Circuits and Systems, and Photonics Global Conference. He received his B.Sc. degree in Electrical & Electronic Engineering from Bangladesh University of Engineering Technology in 2013, M.Eng.Sc. degree in Photonics from University of Malaya, Malaysia in 2016 and M.Eng in Electrical Engineering from University of Idaho, ID in 2019.



Vishal Saxena is an Associate Professor in the Electrical and Computer Engineering at the University of Delaware where he directs the Analog Mixed-Signal and Photonic Integrated Circuits (AMPIC) lab. He obtained his B. Tech. degree in Electrical Engineering from Indian Institute of Technology, Madras in 2002 and M.S. and Ph.D. from Boise State University, ID in 2007 and 2010 respectively. Dr. Saxena is a recipient of 2015 NSF CAREER, 2016 AFOSR Young Investigator Program (YIP), and 2019 DARPA Young Faculty Award (YFA)

awards. He is a member of IEEE and was an Associate Editor for IEEE TCAS-II journal from 2013-15 and 2017-2019. He currently serves on the steering committee of IEEE MWSCAS conference and ISCAS VLSI Committee. His research interests include CMOS photonic interconnects, RF and mmWave Photonic ICs, Data converters, and Neuromorphic computing and low-power circuits for Edge-AI.